Near Real-Time InSAR Deformation Time Series Estimation With Modified Kalman Filter and Sequential Least Squares

Baohang Wang, *Student Member, IEEE*, Qin Zhang, *Member, IEEE*, Chaoying Zhao, *Senior Member, IEEE*, Antonio Pepe, *Senior Member, IEEE*, and Yufen Niu

***Abstract*—The current and planned synthetic aperture radar (SAR) sensors mounted on satellite platforms will continue to operate over the coming years, providing unprecedented SAR data for monitoring wide-range surface deformations. The near real-time processing of SAR interferometry (InSAR) data for the retrieval of ground-deformation time series is urgently required in the current era of big data. The state-of-the-art Kalman filter (KF) and sequential least squares (SLS) algorithms have been proposed to update an InSAR-driven ground-deformation time series. As a contribution of this study, we customize the conventional KF and SLS for big InSAR data for near real-time processing. The development of an accurate prediction model for KF-based InSAR processing is a challenge owing to the large scale of the targets for surface monitoring. We developed a modified KF algorithm, abbreviated as npKF, that does not require any prediction information, abbreviated as npKF. In this context, to avoid occupying a large storage space in SLS-based InSAR processing, we developed a modified SLS algorithm with a truncated cofactor matrix, abbreviated as TSLS. Using both simulated and actual SAR data, we evaluated the performance of these methods under three different aspects: accuracy, computation, and storage performance. With big data, the proposed method can estimate the deformation time series in near real time. It will be a reliable and effective tool for producing near real-time InSAR deformation products in the coming era of processing big SAR data and will play a part in the geologic hazard routine monitoring and early warning system.**

***Index Terms*—Big synthetic aperture radar interferometry (InSAR) data, deformation time series, Kalman filter (KF), sequential least squares (SLS).**

Manuscript received October 26, 2021; revised January 5, 2022 and February 21, 2022; accepted March 12, 2022. Date of publication March 16, 2022; date of current version March 29, 2022. This work was supported in part by the Natural Science Foundation of China under Grant 41874005, Grant 41929001, and Grant 41731066, and in part by the Fundamental Research Funds for the Central Universities under Grant 300102269303 and Grant 300102269719. *(Corresponding author: Qin Zhang.)*

Baohang Wang, Qin Zhang, and Chaoying Zhao are with the School of Geological Engineering and Geomatics, Chang'an University, Xi'an 710054, China (e-mail: wangbaohang@chd.edu.cn; dczhangq@chd.edu.cn; cyzhao@chd.edu.cn).

Antonio Pepe is with the National Research Council of Italy, Institute for the Electromagnetic Sensing of the Environment (CNR-IREA), 80124 Napoli, Italy (e-mail: pepe.a@irea.cnr.it).

Yufen Niu is with the School of Mining and Geomatic Engineering, Hebei University of Engineering, Handan 056038, China (e-mail: niuyufenpippa@163.com).

Digital Object Identifier 10.1109/JSTARS.2022.3159666

I. Introduction

SPACEBORNE synthetic aperture radar interferometry (InSAR) has been under operation for nearly 30 years and has been widely applied in the investigation of earthquakes [1], active faults [2], land subsidence [3], volcanoes [4], landslides [5], and other geological disasters. It has become an unprecedented tool for earth science studies owing to its wide range of coverage and high sensitivity to surface displacement [6], [7].

Over the past two decades, various multitemporal InSAR (MT-InSAR) algorithms have been proposed for the generation of ground-deformation time series, which can be roughly grouped into two main categories: persistent scatterer interferometry [8] and small baseline subsets (SBAS) methodologies [9], [10]. The former generates a set of single primary image interferograms to explore persistent scatterers, whereas the latter generates a set of multiple primary image interferograms to explore distributed scatterers (DS). The features of typical MT-InSAR algorithms have been well-reviewed in [11] and [12].

Over the past decade, spaceborne radar satellites have been developed. Onboard and planned SAR satellites (see Fig. 1) will provide unprecedented big SAR data and shorten revisiting cycles. Sentinel-1A/B provides continuous SAR images, which has a minimum revisiting interval of 6 days. In future missions, an increasing use of SAR satellites such as Sentinel 1C-1D and NASA-ISRO SAR (NISAR), with longer revisiting intervals than the Sentinel-1 Constellation, will shorten the revisiting cycles.

Such ongoing SAR data can promote disaster mitigation in near real-time. To the best of our knowledge, parallel computation and cloud computing-based processing platforms have been constructed from high performance computing to ensure the fast processing of SAR observation data [13]–[15], along with the automatic monitoring of ground deformations, i.e., LiSAR [16]. High performance computing in satellite SAR interferometry has also been discussed [17].

Based on algorithms applying dynamic processing for SAR data, the sequential filtering method for optimizing the PS/DS-InSAR processing flow [18], DS recognition strategies for InSAR processing [19], and a sequential SAR data registration method have been subsequently proposed for Sentinel1 TOPS SAR data [20], [21]. In addition, Hu *et al.* [22], Wu *et al.* [23],

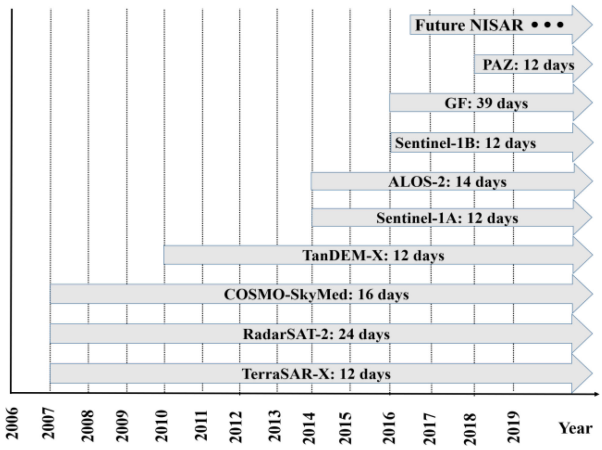

Fig. 1. Onboard and planned SAR satellites.

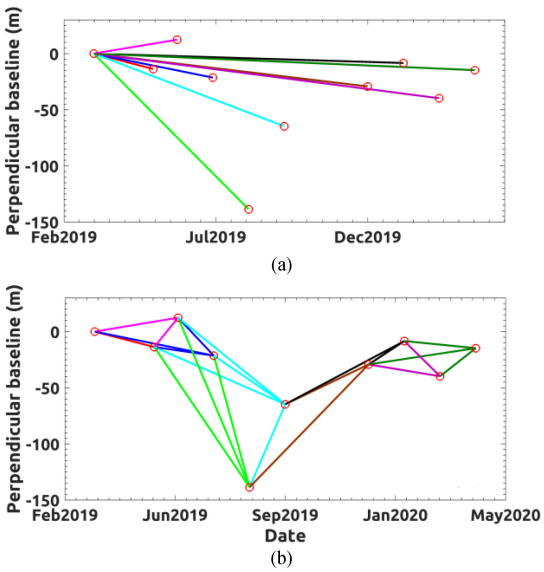

Fig. 2. (a) Single primary and (b) multiple primary image SAR interferograms. Each color line represents a new set of interferograms when we acquire new SAR images one by one.

and Dalaison and Jolivet [24] used a Kalman filter (KF) to update the InSAR deformation time series.

Moreover, to obtain deformation information, Spaans *et al.* and Kelevitz *et al.* [25] proposed near real-time orbit information for radar interferometry. Chen *et al.* [26] also proposed a generic atmospheric correction online service for InSAR.

A. Problem Definition

Biggs *et al.* [27] described how satellite InSAR has evolved from an opportunistic scientific approach to routine monitoring over the past decade. Continuous and dense SAR observation data make it possible to monitor historical deformations, which can enable regulatory agencies to master potential deformation disaster areas and their dynamic changes.

Facing the era of big SAR data, how do we update surface deformation parameters using high-frequency SAR imagery? For PS-InSAR processing, as shown in Fig. 2(a), interferograms represent a wrapped accumulated deformation, and we therefore only need to apply a phase unwrapping to update the deformation time series. However, for SBAS-InSAR, shown in Fig. 2(b), we must recover the cumulative deformation time series from an SBAS interferogram network.

When SAR observation data are quickly obtained, to avoid a deviation of the deformation time series during SBAS-InSAR processing, we must repeatedly invert all unwrapped SB interferograms to obtain accurate ground-deformation time series, which is extremely time-consuming in actual practice.

A KF [22], [23], [24] was proposed to quickly update the deformation time series. However, it is challenging to develop an accurate prediction model for KF-based InSAR processing owing to large-scale targets. An imprecise prediction model may result in an inevitable deviation and affect the accuracy of a subsequent deformation time series [22], [23].

Sequential least squares (SLS) [28], [29], complex SLS for pixel offset SBAS [30], and robust SLS for multisensor InSAR data approaches [31] have been proposed to deal with this problem. However, for SLS processing, we must save the cofactor matrix of the ground-deformation time series with dimensions of $N \times N$ for each pixel (where N represents the number of SAR data), which consumes a large amount of storage space as the number of SAR data becomes extremely large in the era of big SAR data [28], [30], [31].

The main objective of this study is to process big SAR data in near real-time to improve the practicability of an InSAR-driven ground-deformation time series estimation. To this end, we developed a modified SLS method with a truncated cofactor matrix (hereafter, TSLS) and a modified KF without prediction information (hereafter, npKF). The derivation of the two methods is given in the following, and both simulated and actual SAR data are used to evaluate the performance of these two methods with respect to the other three advanced approaches (SBAS, KF, and SLS) in terms of the deformation time series update in a dynamic step-by-step manner.

The rest of this article is organized as follows. Sections II and III describe the near real-time InSAR deformation time series algorithms and their differences. The performances of the two methods are evaluated in Section IV. Finally, a discussion and some concluding remarks are presented in Sections V and VI, respectively.

II. Near Real-Time InSAR Deformation Time Series

For the archived SAR dataset, the initialization of the deformation time series is as follows.

I) We use N archived SAR datasets to generate M SB interferograms. We then remove the topographic induced phase using shuttle radar topography mission digital elevation model (DEM) data and the geometric phase.

II) We use the archived SAR data to generate SB interferograms through a spatiotemporal baseline threshold [9] and determine the qualified pixels for each interferogram. We then select a common stable point in each interferogram to maintain the same reference of the phase unwrapping, which is a key step in InSAR processing

[32], [33]. In this study, the STAMPS software package is used to select the coherent pixels and unwrap the SB interferograms [10].

III) The atmospheric phase screen and the orbital errors are corrected for the *M* SB unwrapped interferograms. The terrain-related atmospheric phase was removed from the best-fitting linear relation between the phase delay and topography [34].

IV) The DEM error is estimated based on the relation between the perpendicular baseline and the unwrapped phase [35].

Next, we model a set of *M* unwrapped interferograms as $\boldsymbol{V}_1 = \mathbf{A}_1\boldsymbol{X}_1 - \boldsymbol{L}_1, \mathbf{P}_1$ to estimate the deformation time series under the norm of the least squares as $\boldsymbol{X}_1 = ({\mathbf{A}_1}^T\mathbf{P}_1\mathbf{A}_1)^{-1}{\mathbf{A}_1}^T\mathbf{P}_1\boldsymbol{L}_1$ and its cofactor matrix $\mathbf{Q}_{\boldsymbol{X}_1} = ({\mathbf{A}_1}^T\mathbf{P}_1\mathbf{A}_1)^{-1}$, where subscript $_1$ represents the archived data, and $\boldsymbol{V}_1$, $\mathbf{A}_1$, $\boldsymbol{L}_1$, $\mathbf{P}_1$, $\boldsymbol{X}_1$, and $\mathbf{Q}_{\boldsymbol{X}_1}$ represent the measurement residual, the design matrix, observations (unwrapped interferograms), the weight matrix, the estimated deformation time series, and its cofactor matrix, respectively.

When a new SAR image is achieved, we can update the ground-deformation time series using new unwrapped interferograms coupled with archived SAR deformation time series and their cofactor matrix under the criterion SLS [28].

Next, we introduce two modified KF and SLS methods for near real-time InSAR ground-deformation time series.

A. Modified KF With No Prediction for InSAR

When we acquire a new SAR data, we can generate *n* SB interferograms with the archived *n* SAR imagery by through a spatiotemporal baseline threshold [9]. Steps (I)–(III) are then implemented. In (II), we can use the estimated deformation and the DEM error to reduce the fringes of the interferograms and improve the reliability of the phase unwrapping.

Then, we model the new observations $\boldsymbol{L}_2$ (unwrapped interferograms related to the acquisition of new SAR data) as follows:

$$\boldsymbol{V}_2 = \underbrace{\left[\mathbf{A}_1^{(2)}\boldsymbol{B}\right]}_{\mathbf{A}_2}\underbrace{\begin{bmatrix}\boldsymbol{X}_1^{(2)}\\ Y\end{bmatrix}}_{\boldsymbol{X}_2} - \boldsymbol{L}_2, \mathbf{P}_2 \tag{1}$$

where $\mathbf{A}_1^{(2)}$ and $\boldsymbol{B}$ are the design matrices, $\mathbf{P}_2$ is a weight matrix, and $\boldsymbol{X}_1^{(2)}$ and Y are updated historical deformation time series and the new cumulative deformation at the new SAR acquisition date, respectively.

KF requires the state equation to describe the motion state of the pixel targets, and thus we employ the state equation matrix $\boldsymbol{\Phi}_{2,1}$ to predict the new deformation time series $\bar{\boldsymbol{X}}_2$ and its cofactor matrix $\boldsymbol{Q}_{\bar{X}_2}$using the error propagation theory, as follows:

$$\begin{aligned}\bar{\boldsymbol{X}}_2 &= \boldsymbol{\Phi}_{2,1}\boldsymbol{X}_1\\ \mathbf{Q}_{\bar{X}_2} &= \boldsymbol{\Phi}_{2,1}\mathbf{Q}_{X_1}\boldsymbol{\Phi}_{2,1}^T,\end{aligned} \tag{2}$$

where $\boldsymbol{Q}_{\bar{X}_2} = \mathbf{P}_{\bar{X}_2}^{-1}$ represents the cofactor matrix of the predicted deformation parameters. Therein, we employ the local linear regression model to predict a deformation through the cumulative deformation at $N-2$ and $N-1$ to determine the cumulative deformation at *N* and its cofactor matrix using the error propagation theory presented in (1). The final estimated deformation time series and its cofactor are as follows:

$$\begin{aligned}\boldsymbol{X}_2 &= \bar{\boldsymbol{X}}_2 + \mathbf{J}_2(\boldsymbol{L}_2 - \mathbf{A}_2\bar{\boldsymbol{X}}_2)\\ \mathbf{Q}_{\boldsymbol{X}_2} &= \mathbf{Q}_{\bar{\boldsymbol{X}}_2} - \mathbf{J}_2\mathbf{A}_2\mathbf{Q}_{\bar{\boldsymbol{X}}_2}\\ \mathbf{J}_2 &= \mathbf{Q}_{\bar{X}_2}\mathbf{A}_2^T(\mathbf{A}_2\mathbf{Q}_{\bar{\boldsymbol{X}}_2}\mathbf{A}_2^T + \mathbf{P}_2^{-1})^{-1}\end{aligned} \tag{3}$$

where $\boldsymbol{X}_2$ and $\mathbf{Q}_{\boldsymbol{X}_2}$ are the updated deformation time series and its cofactor matrix, respectively.

However, in large-scale surface deformation areas, it is challenging to describe the deformation pattern at each pixel using the same state equation. The inaccuracy of the prediction model of the KF method will lead to a deviation of the results [22], [23].

We therefore propose a modified KF (i.e., npKF), in which we do not use any *a priori* deformation. Essentially, we use a modified version of (2) to update the deformation time series, in which we only set $\bar{\boldsymbol{X}}_2 = \begin{bmatrix}\boldsymbol{X}_1\\ 0\end{bmatrix}$ and $\boldsymbol{Q}_{\bar{\boldsymbol{X}}_2} = \begin{bmatrix}\boldsymbol{Q}_{\boldsymbol{X}_1} & 0\\ 0 & \text{inf}\end{bmatrix}$, where inf indicates that the *a priori* information can be ignored. Therefore, the npKF will not be affected by the errors in the predictive information.

Note that the element of the design matrix $\mathbf{A}_1^{(2)}$ includes values of 1 and -1 to indicate whether new data are included in the *n* archived SAR dataset to generate *n* new interferograms. The design matrix is $\mathbf{A}_1^{(2)}$ with dimensions of $(n) \times (n)$. The npKF method can be used as a conventional truncated network to dynamically update the deformation time series.

B. Modified SLS With Truncated Cofactor Matrix for InSAR

According to the SLS estimation theory [29], The final estimated deformation time series and its cofactor are as follows:

$$\underbrace{\begin{bmatrix}\boldsymbol{X}_1^{(2)}\\ Y\end{bmatrix}}_{\boldsymbol{X}_2} = \begin{bmatrix}\boldsymbol{X}_1 + \mathbf{J}_x(\boldsymbol{L}_2 - \mathbf{A}_1^{(2)}\boldsymbol{X}_1 - \mathbf{B}\,Y)\\ (\mathbf{B}^T{\boldsymbol{Q}_J}^{-1}\mathbf{B})^{-1}\mathbf{B}^T{\boldsymbol{Q}_J}^{-1}(\boldsymbol{L}_2 - \mathbf{A}_1^{(2)}\boldsymbol{X}_1)\end{bmatrix},$$

$$\boldsymbol{Q}_{\underbrace{\begin{bmatrix}\boldsymbol{X}_1^{(2)}\\ Y\end{bmatrix}}_{\boldsymbol{X}_2}} = \begin{bmatrix}\boldsymbol{Q}_{\boldsymbol{X}_1^{(2)}} & \boldsymbol{Q}_{\boldsymbol{X}_1^{(2)},\mathrm{Y}}\\ {\boldsymbol{Q}^T}_{\boldsymbol{X}_1^{(2)},\mathrm{Y}} & \boldsymbol{Q}_Y\end{bmatrix} \tag{4}$$

where the unknown elements in (5) can be expressed as follows:

$$\begin{aligned}\boldsymbol{Q}_{\boldsymbol{X}_1^{(2)}} &= \boldsymbol{Q}_{\boldsymbol{X}_1} - \mathbf{J}_x\mathbf{A}_1^{(2)}\boldsymbol{Q}_{\boldsymbol{X}_1} + \mathbf{J}_x\mathbf{B}\boldsymbol{Q}_Y\mathbf{B}^T\mathbf{J}_x^T\\ \boldsymbol{Q}_{\boldsymbol{X}_1^{(2)},\mathrm{Y}} &= -\mathbf{J}_x\mathbf{B}\,\boldsymbol{Q}_Y\\ \boldsymbol{Q}_Y &= (\mathbf{B}^T{\boldsymbol{Q}_J}^{-1}\mathbf{B})^{-1}\\ \mathbf{J}_x &= \boldsymbol{Q}_{\boldsymbol{X}_1}(\mathbf{A}_1^{(2)})^T{\boldsymbol{Q}_J}^{-1}\\ \boldsymbol{Q}_J &= P_2^{-1} + \mathbf{A}_1^{(2)}\boldsymbol{Q}_{\boldsymbol{X}_1}(\mathbf{A}_1^{(2)})^T.\end{aligned} \tag{5}$$

Note that if the new data are included in *n* archived SAR images to generate *n* interferograms, the design matrix $\mathbf{A}_1^{(2)}$ in (1) has $(n) \times (N)$ dimensions with element -1 and 0, while $\boldsymbol{B}$

has $(n) \times (1)$ dimensions with 1, and the cofactor matrix has $(N) \times (N)$ dimensions.

To achieve completely consistent results with the least squares method, we must adopt all deformation time series and their cofactor matrices to update the new deformation time series for each pixel. As shown in (1), increasing the number of SAR data N results in increasing dimensions of the design matrix and cofactor matrix for each pixel, which will occupy a huge storage space and results in low computational efficiency.

To solve this issue, we develop a modified SLS method (i.e., TSLS) with a truncated cofactor matrix, in which we only use part of the archived deformation time series and its cofactor matrix to update the new deformation time series and correct part of the archived deformation time series instead of all the SAR deformation time series and their cofactor matrices. This indicates that the dimensions of the design matrix and the cofactor matrix will not increase for each pixel with the increase in the number of SAR data, which can significantly improve the computational efficiency.

III. Difference Analysis

In the theory of near real-time deformation estimations of big SAR data, we combine the n new unwrapped interferograms, the archived SAR deformation time series, and their cofactor matrices to estimate the deformation time series. It is necessary to analyze the difference between the two new strategies (npKF and TSLS) proposed in this article and three advanced approaches (SBAS, KF, and SLS) in terms of their accuracy, storage, and computational burden.

A. Accuracy

With the KF method, incorrect prediction information will result in a deviation of the estimated parameters. Otherwise, the accuracy of the deformation time series will be modified. The npKF method effectively avoids incorrect prediction information. However, it uses partial interferograms to update deformation parameters, and does not update all archived deformation time series, as shown in (2).

The estimation accuracy of the deformation time series is equivalent for both the SLS and SBAS approaches. However, owing to the truncated cofactor matrix and deformation time series, the TSLS approach need not correct the deformation time series at the SAR acquisition dates when SAR images are not involved in the sequential processing. Therefore, for TSLS, the accuracy of the deformation time series is limited to the dimensions of the truncated cofactor matrix and the deformation time series.

B. Storage Volume

During SLS processing, we use the entire archived deformation time series (N) and its cofactor matrix ($N \times N$) to update new deformation time series and correct all archived deformation time series. However, for the KF, npKF, and TSLS methods, we use a part of the archived deformation time series (n) and its cofactor matrix ($n \times n$) to update the new deformation time series and correct a part of the archived deformation time series.

C. Computational Burden

The SBAS method solves the inversion of a large matrix formed by all unwrapped interferograms, and thus the time consumption of the SBAS method is the largest. However, the KF, npKF, SLS, and TSLS methods only solve the inversion of an obviously small matrix because only a small number of unwrapped interferograms are involved. The time consumption of these four methods is quite small. The SLS method accounts for all archived deformation time series and their cofactor matrices to update the deformation time series at the new SAR acquisition date, and the time consumption of the SLS method is higher than that of the remaining three methods. Meanwhile, the KF, npKF, and TSLS methods use only parts of the deformation time series and their cofactor matrices to update the deformation time series at the new SAR acquisition date. Consequently, their time consumptions are similar but much smaller than the two methods mentioned previously.

Table I summarizes the differences among the SBAS, SLS, TSLS, KF, and npKF in terms of accuracy, storage, and computational burden. In fact, we can set the maximum value to control the dimensions of the stored cofactor matrices.

IV. Performance Analysis

In this section, we discuss the performance of two modified approaches, i.e., npKF and TSLS with respect to three other advanced approaches, i.e., SBAS, KF, and SLS, for the near real-time InSAR deformation time series estimation, in terms of accuracy, storage, and computational burden.

A. Accuracy Analysis of Simulated Data

First, to demonstrate the accuracy of the SBAS, SLS, TSLS, npKF, and KF, methods, for one generic pixel, we simulate three deformation models, including linear, periodic, and mixed deformation models. In total, we consider 169 single look complex (SLC) images, with which we generate 1484 interferograms. Specifically, we assume that the first 20 SLC images are archived data, after which we update the deformation time series in a step-by-step manner from the 21st SLC image to the 169th SLC image. Fig. 3 shows three simulated deformation models with and without noise.

Fig. 3(a), (c), and (e) show the linear, periodic, and mixed deformation time series without noise, respectively. For the linear pattern, all five deformation time series are consistent. However, for the periodic and mixed deformation patterns, the KF method uses the imprecise predictive deformation based on a local linear prediction model, which results in deviations in the deformation time series. The remaining four methods can obtain a consistent deformation time series.

Fig. 3(b), (d), and (f) show the linear, periodic, and mixed deformation time series with noise levels $N\ (0,\ 10^2)$, respectively. We used the local linear prediction model to predict the deformation for KF, which leads to the largest deviations of the deformation time series. Then, the npKF derived deformation time series has smaller deviations than the KF method. The SLS and TSLS methods have the smallest deviations compared with KF and npKF.

TABLE I
DIFFERENCES OF TWO MODIFIEDS AND THREE EXISTING METHODS FOR UPDATING DEFORMATION TIME SERIES

Methods	Accuracy	Time consumption	Storage volume
SBAS	High	slow	All qualified interferograms
SLS	High	Fast	New interferograms and all deformation time series and cofactor matrix
TSLS	Low (limited to the dimension of the truncated cofactor matrix and deformation time series)	Fast	New interferograms and part deformation time series and cofactor matrix
KF	Low (limited to the accuracy of the prediction information deformation time series)	Fast	New interferograms and part deformation time series and cofactor matrix (including predictive part)
npKF	Low (lower than that of TSLS and limited to the dimension of the truncated cofactor matrix and deformation time series)	Fast	New interferograms and part deformation time series and cofactor matrix

TABLE II
STANDARD DEVIATIONS OF ESTIMATED DEFORMATION PATTERNS AT DIFFERENT NOISE LEVELS FOR DIFFERENT METHODS

Methods	Deformation pattern	Standard deviation at different noise levels (mm)			
		N (0, 0)	N (0, 5^2)	N (0, 10^2)	N (0, 50^2)
SLS/SBAS	Linear	0	1.8614	3.7499	18.7131
	Periodic				
	Mixed				
TSLS	Linear	0	1.8615	3.7501	18.7133
	Periodic				
	Mixed				
KF	Linear	0	1.9363	3.9353	19.7379
	Periodic	14.3595	14.4942	14.9042	24.7877
	Mixed	11.1176	11.2959	11.8032	22.9356
npKF	Linear	0	2.2263	4.5072	22.3336
	Periodic				
	Mixed				

Moreover, we evaluate the accuracy of the two modified approaches (npKF and TSLS), compared with the other three advanced approaches (SBAS, KF, and SLS). We conducted 1000 simulations to estimate the standard deviation (STD) of the deformation time series, as shown in Table II. This shows that for any deformation pattern, the STD of the SLS method equals that of the SBAS method. The STD of the npKF method is higher than that of the TSLS approach. The difference in STDS between SLS and TSLS is insignificant. In addition, we find that the accuracy of the deformation time series is unaffected by the models in SLS, TSLS, and npKF.

As shown in Table II, the TSLS and npKF methods have a small deviation. Therefore, we calculate the difference between the npKF and SBAS methods, and that between the TSLS and SBAS methods under different noise levels: $N(0, 5^2)$, $N(0, 10^2)$, and $N(0, 50^2)$, based on the 1000 simulations using mixed models, as shown in Fig. 4. We found that, even at extremely high noise levels, the TSLS method can still achieve an accuracy close to that of the SBAS method with the maximum difference less than 0.08 mm. However, the npKF method has the maximum difference of STD as large as 18 mm.

The newly developed npKF and TSLS methods use a truncation of SB interferogram networks to update the deformation time series. The accuracy of deformation time series is limited to the involved archived SAR data and their cofactor matrices. We show the STD of different numbers of the involved archived SAR data when updating the deformation time series, as shown in Fig. 5. Specifically, Fig. 5(a) and (b) are deviations in the deformation time series corresponding to the npKF and TSLS methods, respectively, when updating the deformation time series with different noise levels and different numbers of archived SAR data.

We estimate the STD between the npKF and SBAS methods, and the STD between the TSLS and SBAS methods across 1000 simulations, as shown in Fig. 5(a) and (b). Specifically, the deformation pattern is from a mixed deformation time series (including linear, exponential, and periodic modes) with different noise levels of $N(0, 5^2)$, $N(0, 10^2)$, and $N(0, 50^2)$, as indicated in Fig. 6. The increasing number of archived SAR images and their cofactor matrices results in a decreased deviation of the estimated deformation time series. The TSLS method has a small deviation at the submillimeter scale, even if the archived SAR

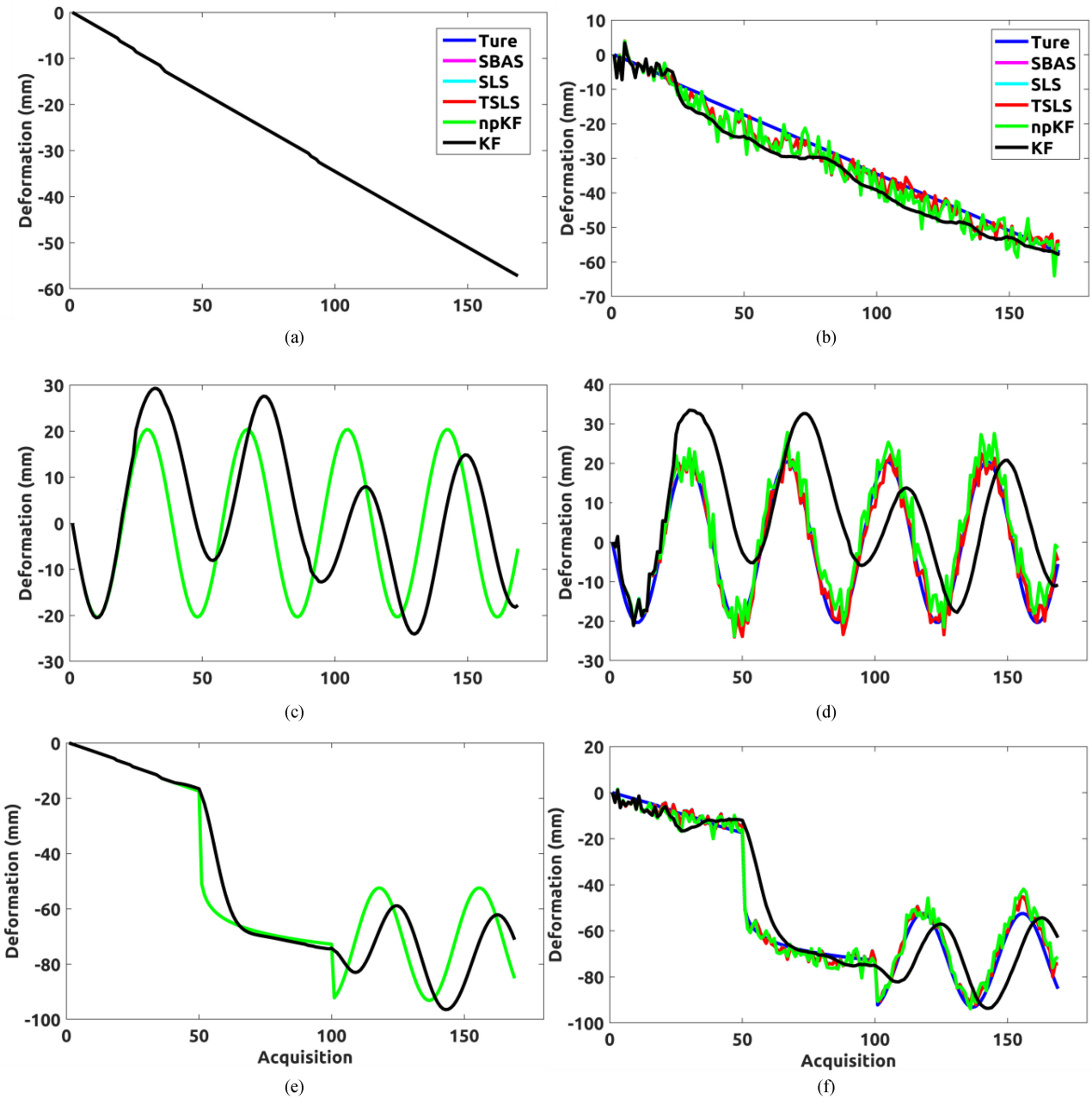

Fig. 3. Simulated1484 multiple primary image SAR interferograms and different deformation time series patterns derived by SBAS (pink line), SLS (light green line), TSLS (red line), npKF (green line), and KF (black line) methods, respectively, in which the blue line is the known deformation time series. The first and second columns represent noise-free and noise-contaminated deformation time series, respectively. (a) and (b) Linear deformation patterns. (c) and (d) Periodic deformation patterns. (e) and (f) Mixed deformation patterns.

images are only from 20 scenes. However, the npKF method has as large deviation at the centimeter level. In addition, the deviation of the deformation time series increases as the amount of noise of the interferograms increases.

B. Accuracy Analysis of Real Data

We demonstrate the accuracy of the KF, npKF, SLS, TSLS, and SBAS methods using real SAR data from Xi'an, China. We employed 46 samples of TerraSAR-X data from the years 2011 to 2015. Fig. 7 shows a spatiotemporal baseline combination, in which the green lines represent the new interferograms for updating the deformation time series related to the new SAR acquisition date.

We consider the first 20 SLC images as archived data, after which we update the deformation time series one-by-one from the 21st SLC image to the 46th SLC image using the KF, npKF, SLS, TSLS, and SBAS methods, respectively. Fig. 8(a) shows the cumulative vertical deformations from 2011 to 2015 using the SBAS approach. Fig. 8(b) and (c) show the difference between the SBAS and SLS, and its histogram, respectively. The results indicate that the SBAS and SLS methods achieve

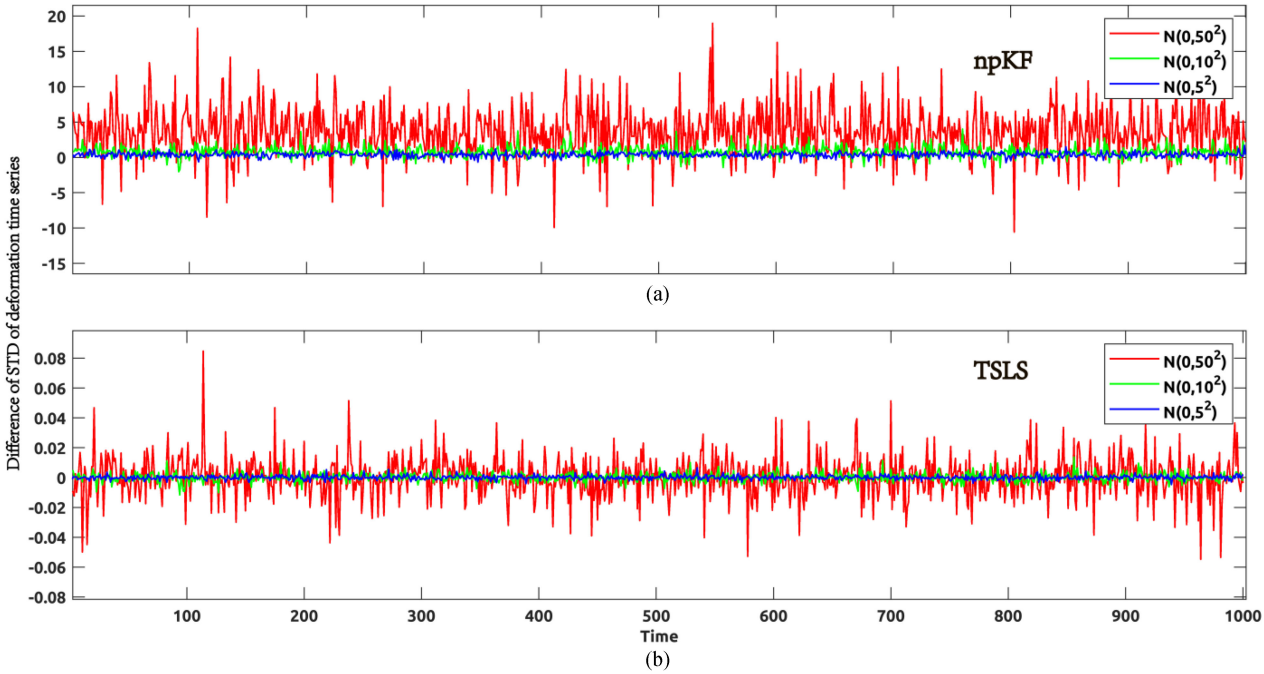

Fig. 4. Difference in STD of deformation time series. (a) Difference of STD between npKF and SBAS methods. (b) Difference of STD between TSLS and SBAS methods, which are estimated under different noise levels: $N(0, 5^2)$, $N(0, 10^2)$, and $N(0, 50^2)$ by conducting 1000 simulations with the mixed models, as shown in Fig. 3(f).

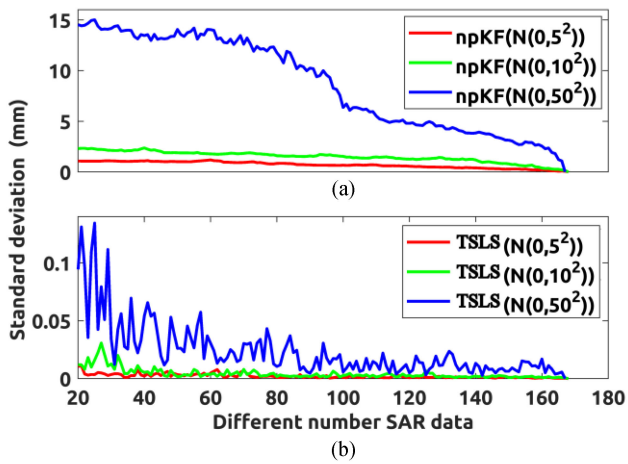

Fig. 5. Deviation in the deformation time series under different numbers of SAR data when updating the deformation time series for different noise levels. (a) and (b) Results of npKF and TSLS methods, respectively.

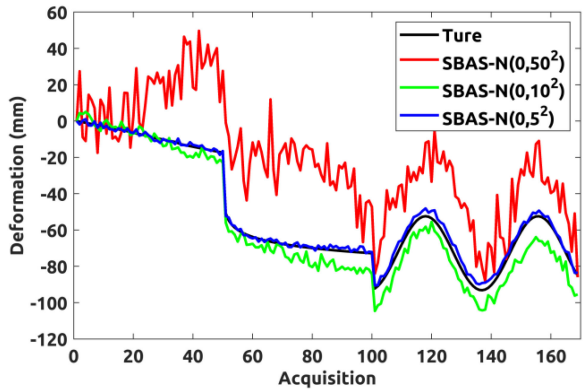

Fig. 6. Deformation time series of mixed models with different noise levels.

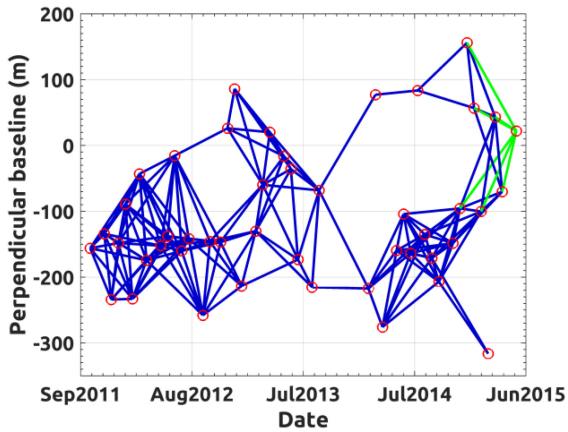

Fig. 7. Spatiotemporal baseline combination for updating deformation time series.

an equal performance. Fig. 8(d) and (e) show the difference between the SBAS and TSLS, and its histogram, respectively, which indicates that a small difference of less than 1 mm occurs. Fig. 8(f) and (g) show the difference between the performances of the SBAS and npKF, i.e., less than 10 mm, and its histogram. Fig. 8(h) and (i) show the difference in performances between the SBAS and KF, i.e., within 40 mm, and its histogram, respectively.

Points P1–P4, highlighted in Fig. 8 are shown in Fig. 9(a)–(d) to compare the deformation time series obtained using the two modified approaches (npKF and TSLS) with the other three

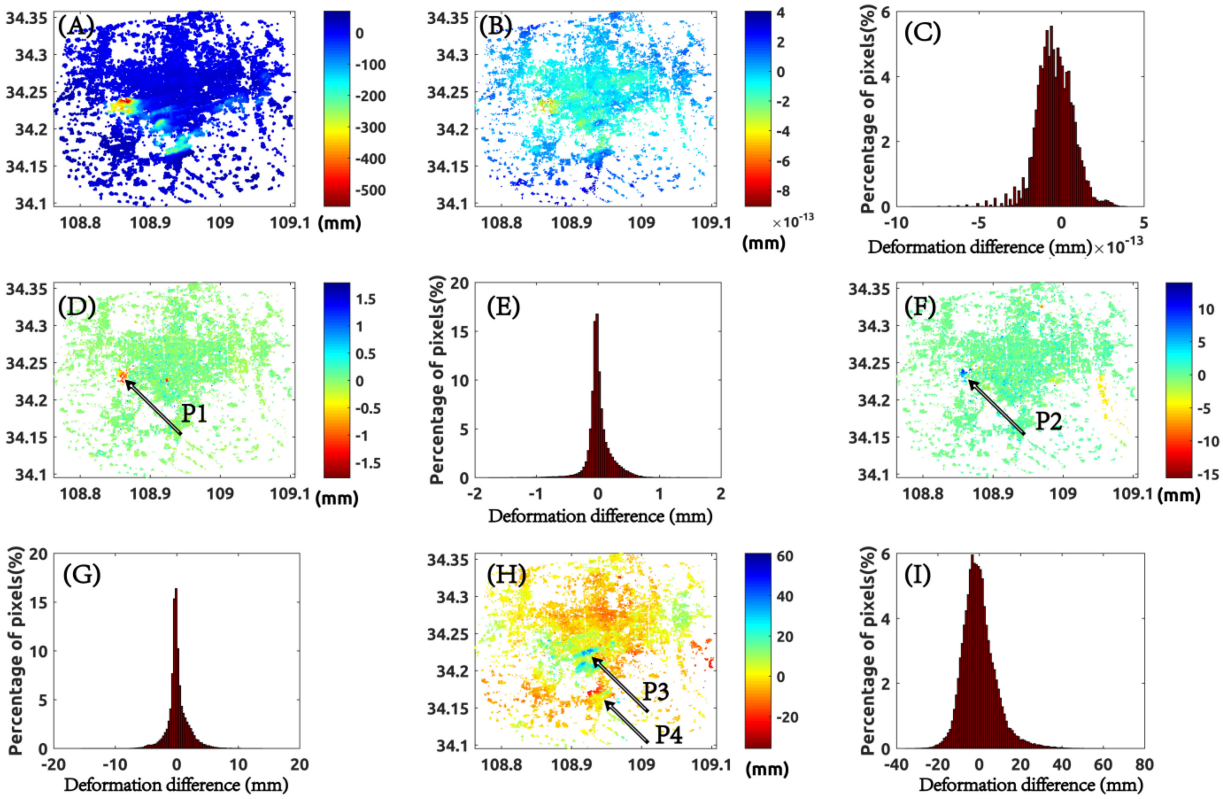

Fig. 8. Comparison of the accuracy of cumulative vertical deformation data from 2011 to 2015. (a) Cumulative vertical deformation obtained using the SBAS method. (b) and (c) Differences between the performances of the SBAS and SLS methods and the corresponding histogram, respectively. (d) and (e) Difference between the performances of the SBAS and TSLS methods and the corresponding histogram, respectively. (f) and (g) Difference between the performances of the SBAS and npKF methods and the corresponding histogram, respectively. (h) and (i) Difference between the performances of the SBAS and KF methods and the corresponding histogram, respectively. Points P1–P4 show the deformation time series presented in Fig. 9.

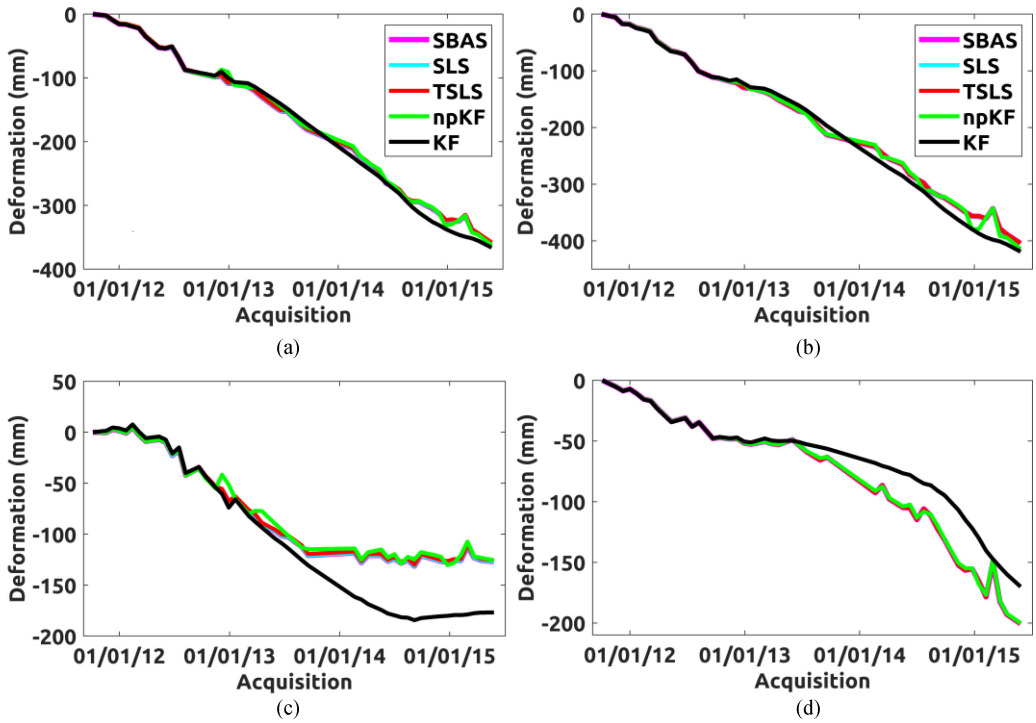

Fig. 9. Deformation time series with different InSAR methods. (a)–(d) Correspond to points P1–P4 in Fig. 8.

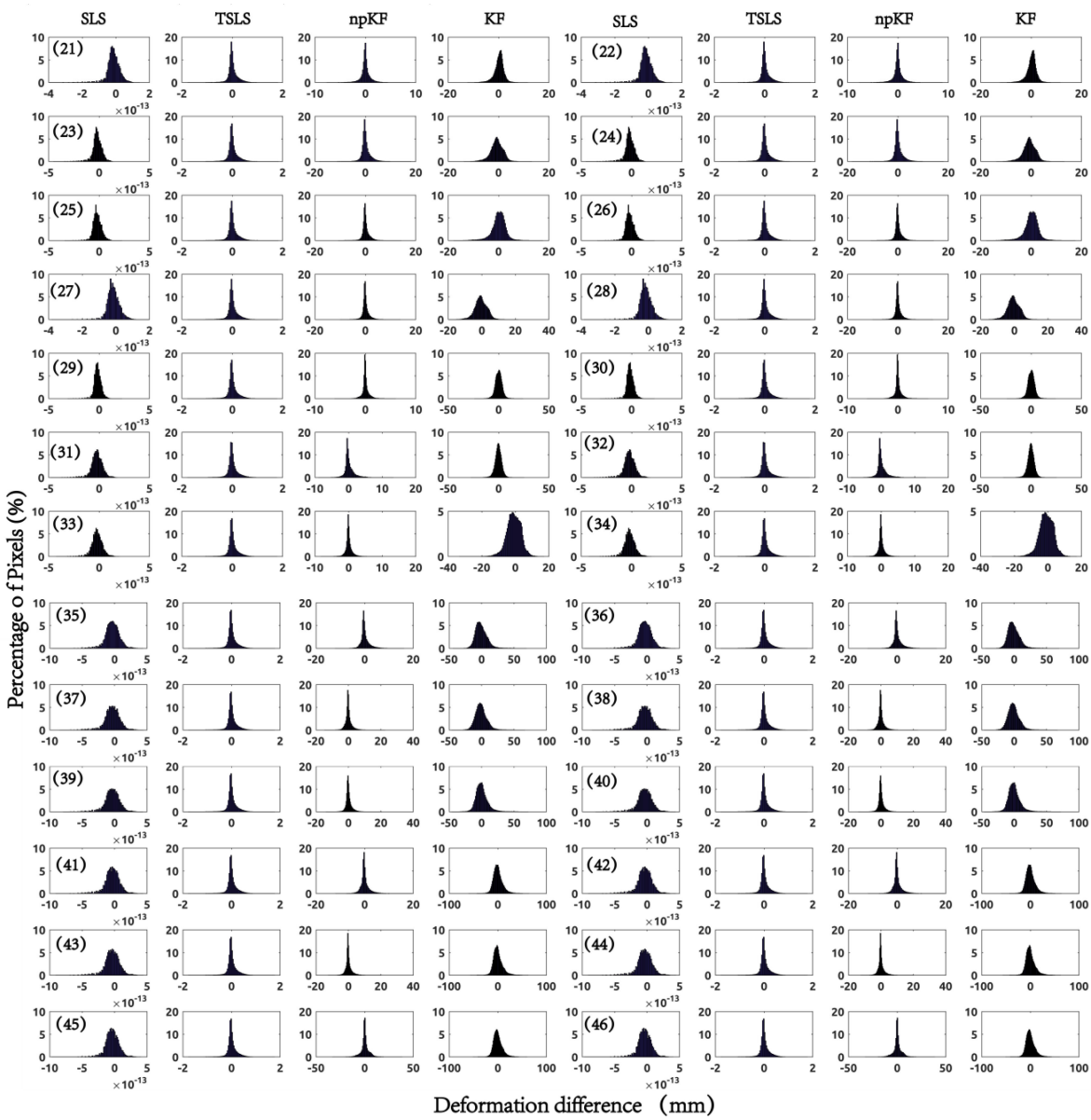

Fig. 10. Histograms of the differences between the SBAS and SLS methods, and among the TSLS, npKF, and KF methods.

advanced approaches (SBAS, KF, and SLS). For the four points, we estimated the STD between the SBAS and SLS methods, SBAS and TSLS methods, SBAS and KF methods, and SBAS and npKF methods.

We use the deformation time series estimated by the SBAS method as a reference. For point P1, the STDs of the deformation time series derived using the SLS, TSLS, npKF, and KF methods are 0, 0.19, 4.50, and 9.68 mm, respectively. For point P2, the STDs are 0, 0.10, 6.03, and 14.16 mm, for point P3, the STDs are 0, 0.20, 4.24, and 26.09 mm, and for point P4, the STDs are 0, 0.00, 0.97, and 15.37 mm, respectively. The incorrect prediction results in a deviation of the estimated parameters during KF-based processing. Although the KF methods have a larger deviation, the TSLS have a small difference in deviation.

Qualitatively, we present histograms of the differences in performances among the SBAS, SLS, TSLS, npKF, and KF methods in Fig. 10, for which the SBAS method was used as the reference value. All the simulated time series, the statistical STD data listed in Table II, the actual data time series, and the actual data histograms presented show that the accuracy of the estimated parameters decreases gradually when using the SLS, TSLS, npKF, and KF methods.

C. Computational Performance Analysis

Herein, we compared the computational efficiency of the newly developed methods (TSLS and npKF) to that of the previously proposed methods (SLS and KF) when updating the deformation time series, as shown in Fig. 11.

We conducted the test using MATLAB R2015b software installed in a computer with an Intel Xeon CPU E5-2640 v4 running at 2.40 GHz. We used 169 samples of SAR data to assess the computing time of these methods when updating the deformation time series for 18 231 pixels.

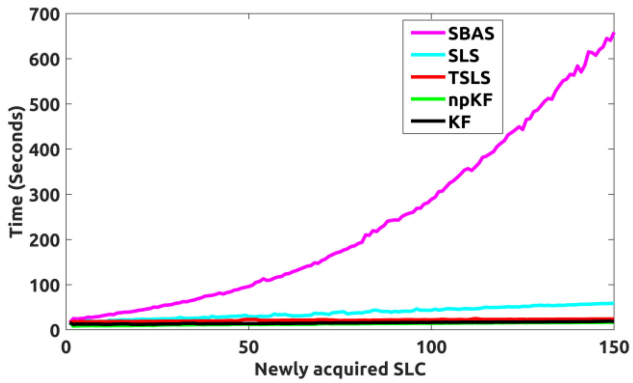

Fig. 11. Comparison of the execution time of the different methods mentioned earlier for the 21st to the 169th SLC images.

As it pertains to updating the deformation time series, the SBAS method consumes the largest amount of time. Because the SLS method requires all archived deformation time series and their cofactor matrices to update a new SAR deformation, the time consumption of the SLS method is higher than that of the TSLS, KF, and npKF methods. Meanwhile, the KF, npKF, and TSLS methods use parts of the deformation time series and their cofactor matrices to update the new SAR deformation time series. As such, their time consumption is similar.

D. Storage Volume Analysis

Owing to the continuous transmission of satellite data and the increasing launches of SAR satellites, increasing SAR data will be acquired, which will inevitably occupy a large storage space. In this section, we compare the storage volume of two modified approaches (npKF and TSLS) with the other three advanced approaches (SBAS, KF, and SLS) in a long-term deformation time series estimation.

We assume that the archived N SAR data are taken to generate M interferograms using the SBAS method. When a new SAR image is acquired, assuming n new interferograms are generated related to the new SAR image, we can then update the deformation time series with the above-mentioned InSAR methods. Specifically, we use all M interferograms for the SBAS-InSAR processing.

However, we use only n new interferograms and N estimated deformation time series and their cofactor matrices with $N \times N$ dimensions for the SLS method. In addition, for KF, npKF, and TSLS, we only consider a small part of the deformation time series (e.g., K) and their cofactor matrices with $K \times K$ dimensions. We concluded that these methods require different data to update the deformation time series shown in Table III.

If the weight matrix of each pixel is equal, the cofactor matrix of all pixels should be the same, which will save a lot of storage space. On the other hand, if the weight matrix of each pixel is different, which we should store each cofactor matrix of each pixel. Fig. 12 shows the storage capability of these methods, from 1 to 500 SLC images, to update the deformation time series. We generated 20 SB interferograms by connecting the latest 20 SLC images with the newly acquired SAR image.

TABLE III
QUANTITY OF MAIN PARAMETER FOR UPDATING DEFORMATION TIME SERIES

Method	Interferograms	Archived Deformation time series	Cofactor matrix
SBAS	M	0	0
SLS	n	N	$N \times N$
TSLS	n	K	$K \times K$
npKF	n	K	$K \times K$
KF	n	K	$K \times K$

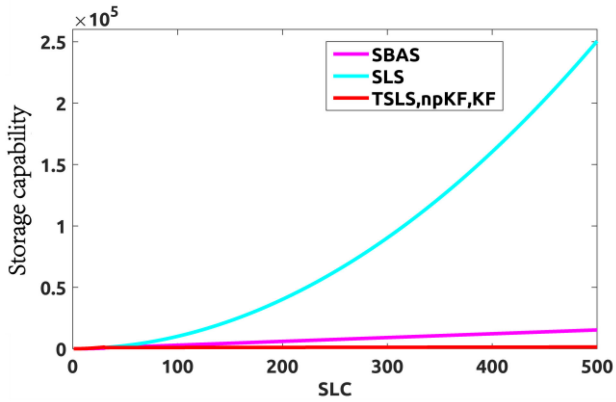

Fig. 12. Comparison of storage capability (including interferograms, archived deformation time series, and cofactor matrix) for 1 to 500 SLC images.

V. APPLICABILITY ANALYSIS

When reliable *a priori* deformation information is available, it is better to use the KF method because the reliable *a priori* information can improve the accuracy of the deformation parameters. However, if the prediction information is biased owing to unreliable *a priori* information, significant bias will be introduced for the KF method. In this case, we first choose the SLS method to update the deformation time series because it is equivalent to the least squares method (SBAS). With an increase in the number of SAR data, to reduce the storage space of the cofactor matrix, it is better to use the TSLS method rather than the npKF method because the deviation of npKF method is larger than that of the TSLS approach.

In practice, to reduce the storage space, we can set the maximum number of archive SAR data K involved when updating the deformation time series, which means that the TSLS method only stores the cofactor matrices of the deformation time series with $K \times K$ dimensions, as shown in Table III, regardless of the N SAR images and M interferograms.

We use the deformation time series of archived SAR data and their cofactor matrices instead of all archived unwrapped interferograms to update the deformation time series, which is suitable for big SAR data processing. To this end, the TSLS method can obtain smaller deviations than the KF and npKF methods to relieve the cofactor matrices with a large number of dimensions. Therefore, the TSLS method will be a promising and effective tool in the coming era of big SAR data processing.

VI. Conclusion

In this study, we propose two new methods, i.e., npKF and TSLS, to estimate the near real-time deformation time series with an increase in the SAR data. We compare the performance of two new methods with three advanced InSAR approaches for updating the deformation time series in terms of the accuracy, storage volume, and time consumed. Moreover, the accuracy of the estimated deformation time series achieved by the TSLS method is higher than that of the KF and npKF approaches. We can conclude that the TSLS method can obtain the deformation time series in near real time with an extremely small difference in comparison with that of the SLS method when large cofactor matrices of the deformation time series for each pixel are not considered. The TSLS approach achieves a good compromise between execution time and accuracy. Both the simulated and real SAR data verify high level performance of the TSLS method, which can be used in the coming era of big SAR data owing to its small storage space, high efficiency, and acceptable level of accuracy.

Acknowledgment

The TerraSAR-X data are copyrighted by the European Space Agency.

References

[1] D. Massonnet, "The displacement field of the landers earthquake mapped by radar interferometry," *Nature*, vol. 364, no. 6433, pp. 138–142, 1993.

[2] T. J. Wright, B. Parsons, P. C. England, and E. J. Fielding, "InSAR observations of low slip rates on the major faults of Western Tibet," *Science*, vol. 305, no. 5681, pp. 236–239, 2004.

[3] G. W. Bawden, W. Thatcher, R. S. Stein, K. W. Hudnut, and G. Peltzer, "Tectonic contraction across Los Angeles after removal of groundwater pumping effects," *Nature*, vol. 412, pp. 812–815, 2001.

[4] Z. Lu and D. Dzurisin, "InSAR imaging of Aleutian volcanoes: Monitoring a volcanic arc from space," in *Springer Praxis Books, Geophysical Sciences*, vol. 390. Berlin, Germany: Springer, 2014, pp. 87–345.

[5] P. Lacroix, A. Dehecq, and E. Taipe, "Irrigation-triggered landslides in a Peruvian desert caused by modern intensive farming," *Nature Geosci.*, vol. 13, no. 1, pp. 50–60, 2020.

[6] R. M. Goldstein and C. L. Werner, "Radar interferogram filtering for geophysical applications," *Geophysical Res. Lett.*, vol. 25, pp. 4035–4038, 1998.

[7] R. Bürgmann, P. A. Rosen, and E. J. Fielding, "Synthetic aperture radar interferometry to measure Earth's surface topography and its deformation," *Annu. Rev. Earth Planet. Sci.*, vol. 28, pp. 169–209, 2000.

[8] A. Ferretti, C. Prati, and F. Rocca, "Permanent scatterers in SAR interferometry," *IEEE Trans. Geosci. Remote Sens.*, vol. 39, no. 1, pp. 8–20, Jan. 2001.

[9] P. Berardino, G. Fornaro, R. Lanari, and E. Sansoti, "A new algorithm for surface deformation monitoring based on small baseline differential SAR interferograms," *IEEE Trans. Geosci. Remote Sens.*, vol. 40, no. 11, pp. 2375–2383, Nov. 2002.

[10] A. Hooper, "A multi-temporal InSAR method incorporating both persistent scatterer and small baseline approaches," *Geophysical Res. Lett.*, vol. 35, pp. 96–106, 2008.

[11] M. Crosetto, O. Monserrat, M. Cuevas-González, N. Devanthéry, and B. Crippa, "Persistent scatterer interferometry: A review," *ISPRS J. Photogramm. Remote Sens.*, vol. 115, pp. 78–89, 2015.

[12] D. H. T. Minh, R. Hanssen, and F. Rocca, "Radar interferometry: 20 years of development in time series techniques and future perspectives," *Remote Sens.*, vol. 12, no. 9, 2020, Art. no. 1364.

[13] C. Wang *et al.*, "First mapping of China surface movement using supercomputing interferometric SAR technique," *Sci. Bull.*, vol. 66, no. 16, pp. 1608–1610, 2021.

[14] I. Zinno, F. Casu, C. D. Luca, S. Elefante, R. Lanari, and M. Manunta, "A cloud computing solution for the efficient implementation of the P-SBAS DInSAR approach," *IEEE J. Sel. Topics Appl. Earth Observ. Remote Sens.*, vol. 10, no. 3, pp. 802–817, Mar. 2017.

[15] P. A. Rosen *et al.*, "The InSAR scientific computing environment," in *Proc. 9th Eur. Conf. Synthetic Aperture Radar*, 2012, pp. 730–733.

[16] M. Lazecký *et al.*, "LiCSAR: An automatic InSAR tool for measuring and monitoring tectonic and volcanic activity," *Remote Sens.*, vol. 12, no. 15, 2020, Art. no. 2430.

[17] P. Imperatore, A. Pepe, and E. Sansosti, "High performance computing in satellite SAR interferometry: A critical perspective," *Remote Sens.*, vol. 13, no. 23, 2021, Art. no. 4756.

[18] H. Ansari, F. De Zan, and R. Bamler, "Sequential estimator: Toward efficient InSAR time series analysis," *IEEE Trans. Geosci. Remote Sens.*, vol. 55, no. 10, pp. 5637–5652, Oct. 2017.

[19] K. Spaans *et al.*, "InSAR processing for volcano monitoring and other near-real time applications," *J. Geophysical Res., Solid Earth*, vol. 121, no. 4, pp. 1947–1960, 2016.

[20] B. Xu, Z. Li, Y. Zhu, J. Shi, and G. Feng, "Kinematic coregistration of sentinel-1 TOPSAR images based on sequential least squares adjustment," *IEEE J. Sel. Topics Appl. Earth Observ. Remote Sens.*, vol. 13, pp. 3083–3093, Jun. 2020.

[21] Z. Ma, M. Jiang, and T. Huang, "A sequential approach for sentinel-1 TOPS time-series co-registration over low coherence scenarios," *IEEE Trans. Geosci. Remote Sens.*, vol. 59, no. 6, pp. 4818–26, Jul. 2020.

[22] J. Hu, X. L. Ding, Z. W. Li, J. J. Zhu, Q. Sun, and L. Zhang, "Kalman-filter-based approach for multisensor, multitrack, and multitemporal InSAR," *IEEE Trans. Geosci. Remote Sens.*, vol. 51, no. 7, pp. 4226–4239, Jul. 2013.

[23] S. Wu, X. Ding, and B. Zhang, "Continuous monitoring the ground deformation by a step-by-step estimator in MTInSAR," in *Proc. IGARSS IEEE Int. Geosci. Remote Sens. Symp.*, Jul. 2019, pp. 1994–1997.

[24] M. Dalaison and R. Jolivet, "A Kalman filter time series analysis method for InSAR," *J. Geophysical Res., Solid Earth*, vol. 125, 2020, Art. no. e2019JB019150.

[25] K. Kelevitz, K. F. Tiampo, and B. D. Corsa, "Improved real-time natural hazard monitoring using automated DInSAR time series," *Remote Sens.*, vol. 13, no. 5, 2021, Art. no. 867.

[26] Y. Chen *et al.*, "Generic atmospheric correction model for interferometric synthetic aperture radar observations," *J. Geophysical Res., Solid Earth*, vol. 123, no. 10, pp. 9202–9222, 2018.

[27] J. Biggs and T. J. Wright, "How satellite InSAR has grown from opportunistic science to routine monitoring over the last decade," *Nature Commun.*, vol. 11, no. 1, pp. 1–4, 2020.

[28] B. Wang, C. Zhao, Q. Zhang, Z. Lu, Z. Li, and Y. Liu, "Sequential estimation of dynamic deformation parameters for SBAS-InSAR," *IEEE Geosci. Remote Sens. Lett.*, vol. 17, no. 6, pp. 1017–1021, Jun. 2020.

[29] B. Wang, C. Zhao, Q. Zhang, and M. Peng, "Sequential InSAR time series deformation monitoring of land subsidence and rebound in Xi'an, China," *Remote Sens.*, vol. 11, no. 23, 2019, Art. no. 2854.

[30] B. H. Wang *et al.*, "Update two-dimensional SAR offset tracking deformation time series with complex sequential least squares estimation," *Remote Sens. Lett.*, vol. 12, no. 3, pp. 247–256, 2021.

[31] B. Wang, C. Zhao, Q. Zhang, Z. Lu, and A. Pepe, "Long-term continuously updated deformation time series from multisensor InSAR in Xi'an, China from 2007 to 2021," in *IEEE J. Sel. Topics Appl. Earth Observ. Remote Sens.*, vol. 14, pp. 7297–7309, Jul. 2021, doi: 10.1109/JSTARS.2021.3096996.

[32] H. Yu, Y. Lan, Z. Yuan, J. Xu, and H. Lee, "Phase unwrapping in InSAR: A review," *IEEE Geosci. Remote Sens. Mag.*, vol. 7, no. 1, pp. 40–58, Mar. 2019.

[33] H. Yu and Y. Lan, "Robust two-dimensional phase unwrapping for multi-baseline SAR interferograms: A two-stage programming approach," *IEEE Trans. Geosci. Remote Sens.*, vol. 54, no. 9, pp. 5217–5225, Sep. 2016.

[34] H. Liang, L. Zhang, X. Ding, Z. Lu, and X. Li, "Toward mitigating stratified tropospheric delays in multitemporal InSAR: A quadtree aided joint model," *IEEE Trans. Geosci. Remote Sens.*, vol. 57, no. 1, pp. 291–303, Jan. 2019.

[35] W. Zhang *et al.*, "Improved DEM reconstruction method based on multi-baseline InSAR," in *IEEE Geosci. Remote Sens. Lett.*, vol. 19, pp. 1–5, Apr. 2022, Art. no. 4011505, doi: 10.1109/LGRS.2021.3069239.

[36] Y. Yuanxi, "Robust Bayesian estimation," *J. Geodesy*, vol. 65, no. 3, pp. 145–150, 1991.

Baohang Wang (Student Member, IEEE) was born in Xianyang, China, in 1992. He received the B.S. degree in surveying engineering from Longyan University, Longyan, China, in 2015, and the M.Sc. degree in geodesy and surveying engineering in 2018 from Chang'an University, Xi'an, China, where he is currently working toward the Ph.D. degree.

His research interests include the development of different InSAR methods, including spatiotemporal phase optimization, phase unwrapping, near real-time SAR/InSAR deformation time series updating, signal unmixing and the applications on dynamic deformation monitoring for artificial infrastructure facilities, land subsidence, landslide by multitemporal synthetic aperture radar interferometry.

Qin Zhang (Member, IEEE) received the Ph.D. degree in geodesy from Wuhan University, Wuhan, China, in 2002.

She is currently a Professor of geodesy and survey engineering with Chang'an University, Xi'an, China. She is currently working on the high-precision geodetic data processing and algorithm development including GNSS, and InSAR, and the monitoring and early forecast on geohazards, including land subsidence, ground fissures, and landslide.

Chaoying Zhao (Senior Member, IEEE) received the M.S. and Ph.D. degrees in geodesy and surveying engineering from Chang'an University, Xi'an, China, in 2002 and 2009, respectively.

He is currently a Professor of geodesy and survey engineering with Chang'an University. His research interests include the development of different InSAR methods, including dynamic SAR/InSAR data processing with the sequential least-squares norm, large gradient surface deformation with SAR offset tracking method, and their applications in geohazard identification, monitoring, and mechanism explanations, including land subsidence, ground fissures, landslide, and mining-induced collapse.

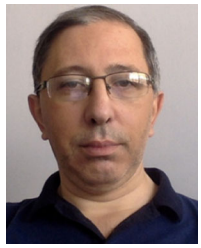

Antonio Pepe (Senior Member, IEEE) received the Laurea degree in electronic engineering and the Ph.D. degree in electronic and telecommunication engineering from the University of Naples Federico II, Naples, Italy, in 2000 and 2007, respectively.

He joined the Istituto per il Rilevamento Elettromagnetico dell'Ambiente, Italian National Research Council (CNR), Naples, where he currently holds a permanent position of Senior Researcher. More recently, he has developed research activities for the generation of DInSAR products through multiplatform/multiangle and the new generation SAR instruments, the generation of hybrid scan SAR-to-stripmap DInSAR analyses, the integration of SAR and optical images, and the analysis of land changes in flooded areas. His main research interests include the development of advanced differential synthetic aperture radar interferometry (DInSAR) algorithms for the monitoring of surface deformation phenomena induced by subsidence, volcano activities, and earthquakes, with a particular interest toward the phase unwrapping problems.

Yufen Niu received the B.S. degree from Hebei University of Technology, Tianjin, China, in 2011, and the M.S. and Ph.D. degrees from Chang'an University, Xi'an, China, in 2015 and 2020, respectively.

From November 2017 to 2019, she was a Visiting Ph.D. Student with Southern Methodist University (SMU), Dallas, USA (supported by China Scholarship Council). Since October 2020, she has been a Lecturer with Hebei University of Engineering, Handan, China. Her research interests related to volcano deformation mapping, magma supply dynamics from InSAR imagery and numerical modeling, landslide monitoring with InSAR and modeling, mapping and characterization of human-induced deformation, co/post/interseismic deformation and seismic slip distribution and fault geometry from InSAR and modeling and wetland monitoring with PolSAR-InSAR.